frontiers | Frontiers in Environmental Science

TYPE Original Research
PUBLISHED 05 September 2024
DOI 10.3389/fenvs.2024.1451496

OPEN ACCESS

EDITED BY
Abdul Qadeer,
Chinese Research Academy of Environmental Sciences, China

REVIEWED BY
Meifang Li,
Central South University Forestry and Technology, China
Qinhe Pan,
Hainan University, China
Shiyu Fu,
South China University of Technology, China

*CORRESPONDENCE
Ying Cao,
yingcao@swust.edu.cn
Shanglian Hu,
hushanglian@swust.edu.cn

RECEIVED 19 June 2024
ACCEPTED 19 August 2024
PUBLISHED 05 September 2024

CITATION
Yang F, Li H, Wang B, Fan W, Gu X, Cao Y and Hu S (2024) Effect of cellulose-lignin ratio on the adsorption of U(VI) by hydrothermal charcoals prepared from *Dendrocalamus farinosus*. *Front. Environ. Sci.* 12:1451496. doi: 10.3389/fenvs.2024.1451496

Effect of cellulose-lignin ratio on the adsorption of U(VI) by hydrothermal charcoals prepared from *Dendrocalamus farinosus*

FanQin Yang, Hanhan Li, Boya Wang, Wei Fan, Xiaoyan Gu, Ying Cao* and Shanglian Hu*

College of Life Sciences and Engineering, Southwest University of Science and Technology, Mianyang, China

Herein, the impact of varying proportions of cellulose/lignin in bamboo on the production of hydrothermal biochar was investigated. Different characterization techniques were applied to explore the structure of hydrothermal biochar derived from three different genotypes (215, 30-A, 52-B) of *Dendrocalamus farinosus*, and the adsorption behavior of uranium by these hydrothermal biochars was evaluated. It was found that a decrease in cellulose/lignin ratio (3.08, 2.68, and 2.58) positively influenced the specific surface area and pore volume of hydrothermal biochar. Consequently, the prepared hydrothermal biochars exhibited adsorption capacities for U(VI) ions at levels of 14.78 mg/g, 24.68 mg/g, and 26.02 mg/g respectively under these three ratios. The adsorption process by 52-B-220 well complied with the Freundlich isotherm, which indicated that the multi-layer adsorption occurred on the solid liquid interface, but single-layer adsorption was evident in those prepared from genotypes 30-A and 215. This study demonstrated that adjusting biomass feedstock composition as an effective strategy for enhance the quality of biochar.

KEYWORDS

cellulose-lignin ratio, *Dendrocalamus farinosus*, hydrothermal biochar, adsorption, uranium

1 Introduction

As the global nuclear industry expands, an increasing number of radionuclides are being released into aquatic environments, posing significant health risks to both wildlife and humans (Hinck et al., 2021; Li et al., 2019; Liu et al., 2023). U(VI), one of the most prevalent radionuclides, has garnered extensive attention owing to its significant radioactivity and toxicity (Domingo, 2001; Liang et al., 2022). Biochar, used as an adsorbent, is widely employed in wastewater treatment processes to remove heavy metal pollutants from water due to its low environmental impact, cost-effectiveness, and superior pore structure (Ahmad et al., 2014). Biochar is produced using various biomass as raw materials, with lignocellulosic biomass being the primary source (Cuong et al., 2021). Variations in lignocellulosic biomass result in distinct physical and chemical properties of biochar (Elnour et al., 2019), thereby influencing its adsorption capacity for U(VI). Consequently, it is imperative to investigate how raw materials influence biochar and subsequently affect its adsorption capacity.

Recent research has extensively explored the formation of biochar. Yu, Titirici, Falco, and colleagues have examined the effects of individual components on biochar formation,

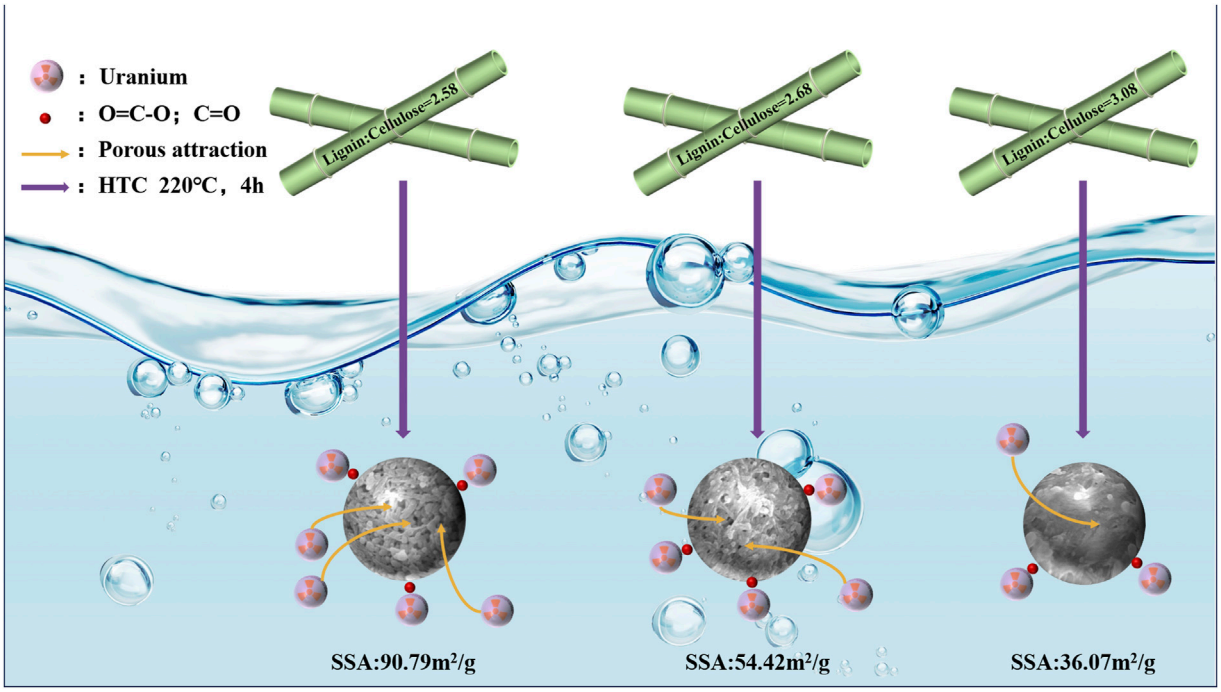

GRAPHICAL ABSTRACT

thereby establishing a theoretical framework for the role of raw materials (Falco et al., 2011; Titirici et al., 2008; Yu et al., 2012). In their pursuit to minimize costs and maximize efficiency, Lawal et al. assessed the influence of cellulose content on the physicochemical properties and adsorption capacity of biochar, utilizing materials such as cellulose, oil palm frond, and palm kernel shell. They concluded that a higher cellulose content significantly enhances the adsorption capacity of biochar (Lawal et al., 2021). However, these investigations primarily concentrated on the impacts of individual components. Biomass materials, principally consisting of cellulose, hemicellulose, and lignin, form the essential structural foundation for post-carbonized biochar. During the preparation of biochar, each polymer is subjected to pyrolysis at varying temperature ranges (Wu et al., 2018; Zhu and Zhong, 2020). Consequently, enhancing the microporous and mesoporous structure of biochar for improved pollutant adsorption necessitates a detailed analysis of the biomass's chemical composition and thermal decomposition properties, particularly the cellulose-lignin ratio.

Bamboo, as a lignocellulosic biomass, is an ideal material for biochar production due to its abundance and renewable nature. In our recent study, we reported the development of novel germplasm resources for *D. farinosus* (Hu, 2022), emphasizing the cultivation of diverse genotypes in our initial experiments. Several mutagenized strains of *D. farinosus* exhibited significant intraspecific variation in chemical composition, allowing us to negate the impact of variability among different lignocellulosic biomasses. Ideal experimental materials derived from these mutagenized strains were used to investigate the influence of chemical components in raw materials on the physicochemical properties and adsorption capacities of biochar.

Consequently, this study aimed to produce biochar from *D. farinosus* with varied cellulose -lignin ratios and to assess the effects of these variations on the physicochemical properties and adsorption capacities of the biochar. An in-depth characterization of various genotypes of *D. farinosus* and their respective biochars was conducted to elucidate the relationship between cellulose -lignin ratios and both the physicochemical properties and the adsorption capacities of the biochar. Based on these insights, it becomes feasible to tailor the physicochemical properties and adsorption capacities of biochar through precise adjustments of the cellulose -lignin ratio.

2 Materials and methods

2.1 Materials

Three genotypes *of D. farinosus* (i.e., 52-B, 30-A, and 215) were provided by the Bamboo Institute of Southwest University of Science and Technology (Sichuan, China). Uranyl nitrate hexahydrate ($UO_2(NO_3)_2{\cdot}6H_2O$), and arsenazo III ($C_{22}H_{18}As_2N_4O_{14}S_2$) were obtained from Rhawn Reagents (Shanghai, China). Other reagents, such as anhydrous ethanol and hydrochloric acid was purchased from Chengdu Jinshan Chemical Reagent Co., Ltd., (Chengdu, China) and Chengdu United Chemical Reagent Research Institute (Chengdu, China), respectively.

2.2 Preparation of hydrothermal charcoals

Bamboo stems were harvested at breast height from the different genotypes of two-year-old *D. farinosus*. All samples were rinsed by deionized water three times and then oven dried at 65°C to ensure consistent weight. The dried bamboo stems were milled by a commercial grinding machine with the powder passing through a 200-mesh sieve. Approximately 4.0 g of each bamboo powder was

transferred to a sealed reactor with 200 mL deionized water, and kept at 220°C for 4 h and then cooled naturally. The processed material was centrifuged at 7500 rpm for 10 min, the liquid was discarded, and the precipitate was repeatedly centrifuged in aliquots of anhydrous ethanol until the supernatant was clear and transparent. Then filtered, neutralized by washing with deionized water and oven-dried at 65°C overnight. The resulting solids from different bamboo samples were marked as 52-B-220, 30-A-220, and 215-220, respectively. where the samples were identified by the genotype of the biomass and the heating temperature. The yield of the hydrothermal charcoal (*Y, %)* was calculated from Equation 1:

$$Y = \frac{M_1}{M_0} \times 100\% \quad (1)$$

M_0(g): the mass of the dry matter;
M_1(g): the mass of the hydrothermal charcoal.

2.3 Characterization of the adsorbents

The surface morphology was observed by Scanning Electron Microscope (SEM, SU8020 instrument, Hitachi, Japan). FTIR spectra were obtained by the KBr pellet method, within the range of 4,000–1,000 cm^{-1} a (Nicolet iS10, Thermo Scientific, United States). Specific surface areas and pore volumes were measured with ASAP® 2,460 Surface Area and Porosimetry System Analyzer (Micromeritics Instrument Corporation, Norcross, GA, United States). Elemental composition was obtained by Vario EL cube elemental analyzer (Elementar, Germany). Zeta equipotential was obtained by Zetasizer Nano ZS90 (Malvern, Britain). The electrochemical reduction of uranium was measured on an electrochemical station (CHI 660E).

2.4 Batch adsorption experiments

To investigated the influence of (a) adsorbent mass (0.02–0.4 g); (b) pH (2–6); (c) contact time (0–24 h); (d) temperature (15°C–55°C); and (e) initial concentration of U(VI) (5–45 mg/L) on U(VI) adsorption performance. First, several solutions of uranyl nitrate were obtained with different concentrations and adjusted to the required pH using NaOH (0.1 M) and HNO_3. Then, the prepared solutions (50 mL) were placed into conical flasks, the adsorbent was then added (as required), and the resulting mixture was reacted in an oscillating (150 rpm) air-bath shaker for predetermined periods of time at the required temperatures. Finally, determination of U(VI) with arsenazoIII as complexing agent, its concentration being determined by absorbance at 520 nm on a T6 New Century UV spectrophotometer (Beijing Puxi General Instrument Co., Ltd., Beijing, China). Overall, repeated three times at each condition, the average concentrations of U(VI) were used for data analysis. The adsorption capacity and removal rate of U(VI) by biochar were used to characterize the adsorption performance of the charcoals; their values were calculated from Equations 2, 3 (Zhao et al., 2017):

$$q_e = \frac{(C_0 - C_e)V}{m} \quad (2)$$

$$\mathrm{RE} = \frac{C_0 - C_e}{C_0} \times 100\% \quad (3)$$

q_e (mg/g): the adsorption capacity;
RE (%):the removal rate at adsorption equilibrium;
C_0 (mg/L): the initial concentration of uranyl ion before adsorption;
C_e (mg/L): the concentration of U(VI) at equilibrium, mg/L; V (L): the volume of the adsorption solution;
m(g): the mass of adsorbent.

2.5 Elution/regeneration study

We conducted an elution/regeneration study using an improved version of the method of Li et al. (2019), to investigate the reusability of 52-B-220 through five adsorption-desorption cycles.

2.6 Statistical analyses

Statistical product and service solutions (SPSS) software (SPSS statistics 22, IBM Corporation) was used to perform the significance analysis between chemical composition. Letters indicate differences in chemical composition of the three genotypes of *D. farinosus* according to Tukey b's honestly significant difference ($p < 0.05$).

3 Results and discussion

3.1 Characterization of the biomass

3.1.1 Composition

The chemical compositions of the three *D. farinosus* genotypes are detailed in Table 1. Among the various raw materials, the largest difference in cellulose content (12%) was observed between genotypes 215 and 52-B. No significant differences in lignin content were observed. Consequently, the cellulose-to-lignin ratio varied significantly across the genotypes. Additionally, the carbon content among the three *D. farinosus* genotypes remained consistent at 44.6%–46.2%, whereas substantial variations in oxygen content were observed, ranging from 30.7% to 40.1% (Table 1). Therefore, the *D. farinosus* genotypes exhibited significant differences both individually and in their relative compositions.

3.1.2 Thermogravimetric analysis

TG (thermogravimetry) and DTG (derivative thermogravimetry) analyses were conducted to evaluate the properties of raw biomass following thermal decomposition (Figure 1). The devolatilization zone (150°C–400°C) for each genotype showed variations in mass loss, ranging from 70.46% (52-B) to 59.08% (215), attributed to the differing compositions of the biomasses. Finally, mass loss within the continuous devolatilization zone (400°C–600°C) ranged from 7.47% (52-B) to 6.45% (30-A).

TABLE 1 Cellulose content, lignin content, cellulose-lignin ratio, and elemental abundance of the three genotypes of *D. farinosus*.

Sample	Cellulose %	Lignin %	Cellulose-lignin	Element abundance %			
				C	H	O	N
52-B	42.4 ± 0.26c	16.4 ± 0.07b	2.58 ± 0.01c	45.3	6.09	40.1	0.38
30-A	43.8 ± 0.38b	16.4 ± 0.20b	2.68 ± 0.03b	44.6	6.10	30.7	0.54
215	53.5 ± 0.06a	17.4 ± 0.36a	3.08 ± 0.06a	46.2	5.87	33.2	0.41

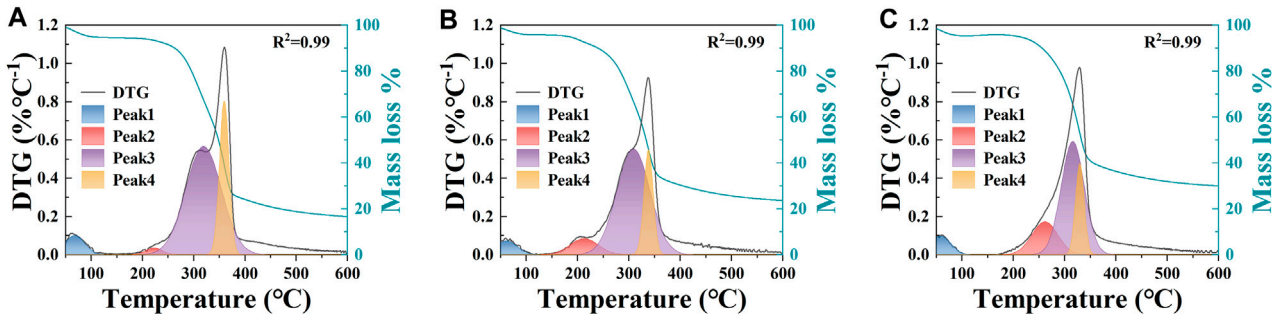

FIGURE 1
TG and deconvolution of the DTG curves showing the peaks due to each component for the three genotypes of *D. farinosus*: **(A)** 52-B; **(B)** 30-A; **(C)** 215.

To determine the optimal hydrothermal temperature for preserving lignin as the structural framework of hydrothermal charcoal and for forming cellulose-associated carbon microspheres, the DTG curve was deconvoluted to isolate the pyrolysis peaks of each component (Wu et al., 2018). The DTG curve revealed four distinct peaks at approximately 60°C (peak 1), 200°C (peak 2), 300°C (peak 3), and 350°C (peak 4), corresponding to moisture, hemicellulose, cellulose, and lignin, respectively (Figure 1). A thorough examination of these component peaks revealed that their pyrolysis onset temperatures varied significantly. Specifically, the pyrolysis onset temperatures were 180°C for hemicellulose, 200°C for cellulose, and 300°C for lignin, consistent with findings from previous studies (Liang et al., 2018; Tong Thi et al., 2014; Yang et al., 2017). Furthermore, during the hydrothermal reaction, the subcritical state of the liquid phase (i.e., water) can accelerate the reaction rate and induce sample corrosion (Zanon Costa et al., 2020). To ensure the complete reaction of hemicellulose and cellulose into carbon microspheres and retention of the lignin-based hydrothermal charcoal framework, a final hydrothermal temperature of 220°C was selected.

3.2 Characteristics of hydrothermal charcoals

3.2.1 Surface morphology and pore structure

SEM images of the hydrothermal charcoals were captured to elucidate the surface morphologies of the three *D. farinosus* genotypes (Figures 2A–C). The agglomeration of carbon microspheres intensified with increasing cellulose/lignin ratios, ultimately resulting in the complete envelopment of the surface. At this final stage, the filamentous structure became indistinguishable, and the pore structure significantly diminished (215–220).

A lignin skeleton with attached carbon microspheres was observed in 52-B-220 (Figure 2A), signifying its superior efficacy in biochar production. This observation is consistent with previous studies that demonstrate the effective cross-linking of hemicellulose, cellulose, and lignin within a three-dimensional matrix (Deanin et al., 1978; Kang et al., 2019). Consequently, the lower cellulose-to-lignin ratio in 52-B likely enhanced the exposure of the polymer network to the processing conditions at 220°C.

The FTIR spectra of the three hydrothermal charcoals are shown in Figure 2D. No significant differences were observed in the peaks associated with functional groups among the three hydrothermal charcoals. The characteristic bands and their corresponding assignments are as follows: 3348 cm^{-1} (broad, O-H stretching vibration); 1700 cm^{-1} [C=O stretching vibrations of aldehyde, ketone, ester, and carboxyl (Fang et al., 2014)]; 1,608 cm^{-1} (C=O stretching vibrations of the benzene ring) and 1,316 cm^{-1} [C-O stretching vibration of the carboxylate anion (Chen et al., 2018)]; 1,265 cm^{-1} (C-O-C and phenolic -OH stretching vibration of aromatic hydrocarbons); 1,160 cm^{-1}, 1,110 cm^{-1}, and 1,058 cm^{-1} (C-O vibrations of ethers, alcohols, phenols). The presence of these characteristic bands indicates that the surface composition of hydrothermal charcoal is predominantly composed of hydroxyl and carboxyl groups. However, the peaks at 1,510 cm^{-1}, 1,425 cm^{-1}, and 1,265 cm^{-1} are attributed to lignin (Aleeva et al., 2020; Liu et al., 2017), indicating that its structure was preserved during the preparation process, a finding consistent with SEM observations.

The yields of hydrothermal charcoals from the three *D. farinosus* genotypes are shown in Figure 2E. No significant differences ($p > 0.05$) were observed in the yields among the three *D. farinosus*

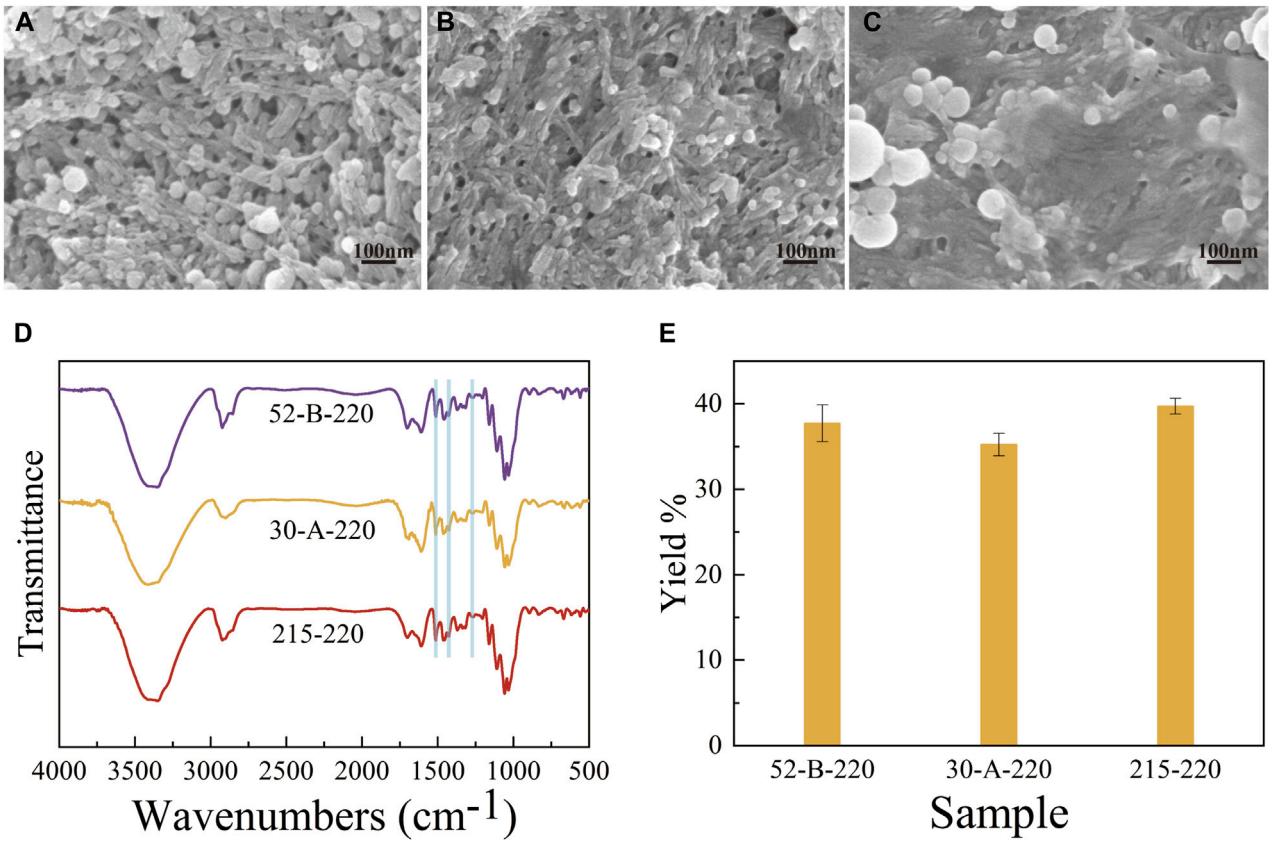

FIGURE 2
The SEM images of hydrothermal charcoals **(A)** for 52-B-220, **(B)** for 30-A-220, **(C)** for 215–220. **(D)** FTIR spectra of hydrothermal charcoals. **(E)** Yields of hydrothermal charcoals.

genotypes, indicating that utilizing *D. farinosus* with low cellulose/lignin ratios for hydrothermal charcoal production is unlikely to raise production costs.

Given that pore structure is a critical factor influencing sorbent adsorption performance, the pore diameters, specific surface areas, and pore volumes of each hydrothermal charcoal are shown in Table 2. No significant differences were observed in the pore diameters among the three-genotype charcoals, while specific surface areas and pore volumes decreased with increasing cellulose/lignin ratios. This phenomenon can be attributed to the increase in carbon microsphere formation, as cellulose is the primary precursor for these structures (Sevilla and Fuertes, 2009; Titirici et al., 2008). The subsequent agglomeration of excess carbon microspheres blocks the formation of new pores or constricts existing ones, leading to a reduction in specific surface area and pore volume (Yu et al., 2012).

3.3 Adsorption performance

3.3.1 The effect of experimental parameters on adsorption

pH is a crucial factor in adsorption processes as it significantly influences charge transfer at the solid–liquid interface (Fang et al., 2020). Consequently, it is imperative to systematically investigate the effect of pH on U(VI) adsorption (Hui et al., 2019). The surface charge of the adsorbent was evaluated across a pH range of 2.0–8.0, while the adsorption performance of hydrothermal charcoals was assessed at pH 2.0–6.0. The surface charge of the adsorbent continues to decline until pH 6.0 (Supplementary Figure S1), indicating that the adsorbent surface is severely protonated at low pH. That leads to adsorption competition between UO_2^{2+} and H^+, as well as electrostatic repulsion occurred between the adsorbent and UO_2^{2+}. As pH increases, protonation weakens, and the adsorption capacity of the adsorbent gradually increases (Zhao et al., 2017). Additionally, when the pH exceeds 5.0, the species of U in the solution change and begin to form precipitates rather than adsorb, leading to a decrease in adsorption capacity (Liao et al., 2022). This observation is consistent with the results shown in Figure 3A and those reported in previous studies (Abdi et al., 2017; Humelnicu et al., 2014). Therefore, pH 5.0 is considered more suitable for U(VI) adsorption.

Furthermore, Figure 3B illustrates the influence of contact time, ranging from 0 to 300 min, on the adsorption capacity of the hydrothermal charcoals. The adsorption of U(VI) increased rapidly during the first 120 min, then gradually slowed as it approached equilibrium at 300 min. This trend is consistent with the decrease in available adsorption sites, which are progressively occupied by U(VI) ions.

Notably, the adsorption capacity of each hydrothermal charcoal exhibited an inverse relationship with the mass of

TABLE 2 Pore diameter, specific surface area, and pore volume measurements were obtained from the analysis of each hydrothermal charcoal.

Sample	Surface area (m^2/g)	Pore volume (cm^3/g)	Average pore diameter (nm)
52-B-220	90.7914	0.198,307	7.5515
30-A-220	54.4164	0.113,982	7.4554
215–220	36.0689	0.077575	7.3017

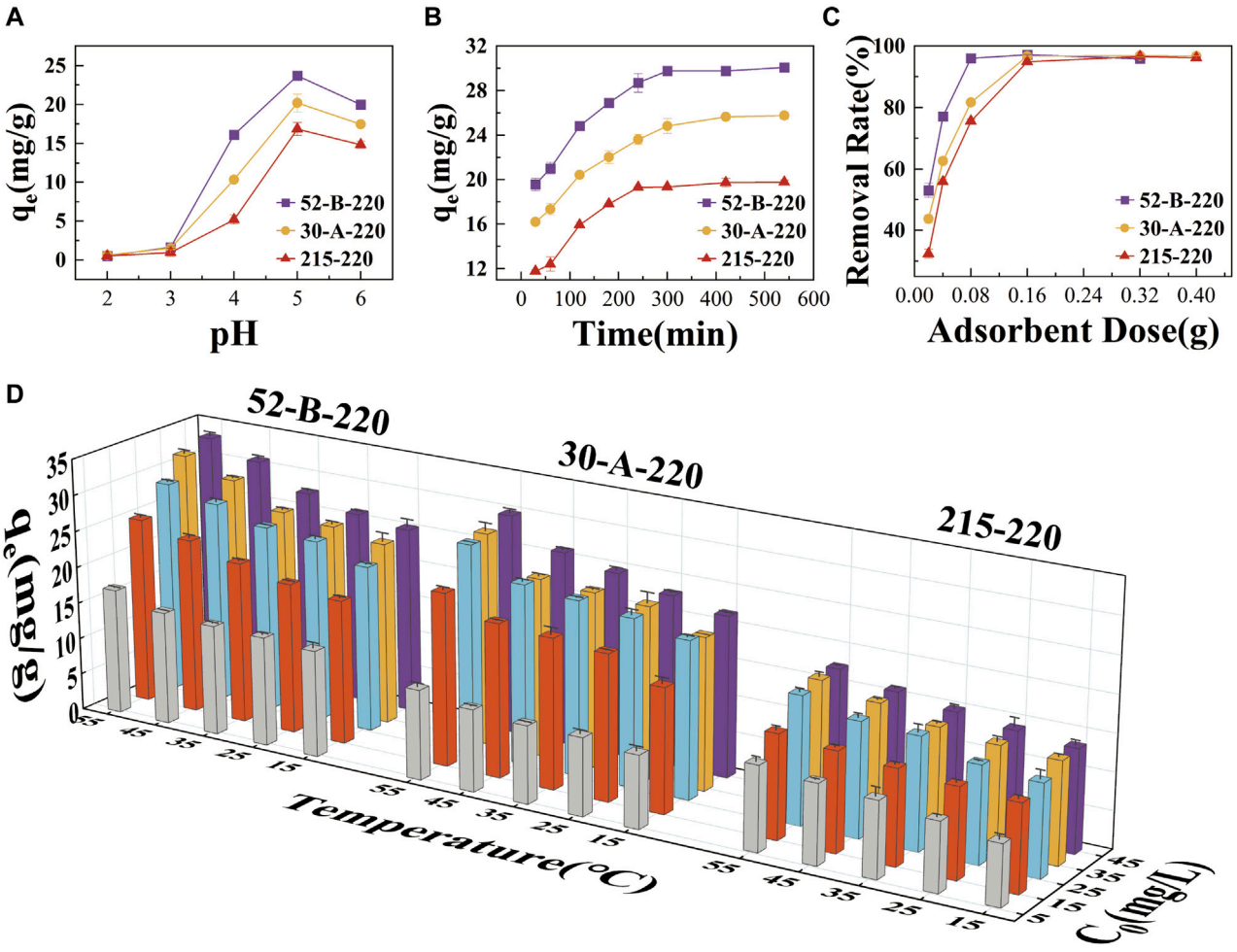

FIGURE 3
(A) Influence of pH on the adsorption capacity of each hydrothermal charcoal. **(B)** Influence of contact time on the adsorption capacity of each hydrothermal charcoals. **(C)** Influence of adsorbent mass on adsorption capacity of each hydrothermal charcoal. **(D)** Effects of initial concentration of U(VI) ions and temperature on the adsorption capacity of each hydrothermal charcoal.

the adsorbent, while their removal rates increased with higher adsorbent masses (>95%) (Figure 3C). The optimal adsorbent masses for 52-B-220, 30-A-220, and 215–220 were determined to be 0.08 g, 0.16 g, and 0.16 g, respectively. The observed increase in removal rate can be attributed to the greater availability of adsorption sites for U(VI) ions due to the increased mass of the adsorbent. Given that a larger specific surface area enhances the adsorption capacity per unit mass, an equivalent removal rate can be achieved with a smaller adsorbent mass. Consequently, 52-B-220 exhibited optimal adsorption performance at the lowest adsorbent mass.

As illustrated in Figure 3D, the effects of a broad temperature range (15°C–55°C) and varying initial concentrations of U(VI) ions (5–45 mg/L) on the adsorption performance of each hydrothermal charcoal were examined. Consistent with published data, the adsorption capacities of each hydrothermal charcoal increased with rising temperature, likely due to the enhanced mass transfer of ions in solution at elevated temperatures. This effect accelerates the mass transfer rate of the adsorbate from the outer layer of the adsorbent to the inner pores (Inyang et al., 2016; Mishra et al., 2006). The adsorption capacity also exhibited a direct correlation with the initial concentration of U(VI) ions, reaching saturation at 35 mg/L.

Previous studies have demonstrated that increasing the initial concentration enhances adsorption capacity by amplifying both the driving force for mass transfer and the contact rate of U(VI) ions with adsorption sites (Wegener et al., 2009). Adsorption saturation was achieved when the concentration of uranyl ions in the solution became sufficient to fully occupy the adsorption sites on the hydrothermal charcoal.

3.3.2 Adsorption kinetics

The adsorption mechanism of U(VI) ions in the solid-liquid system was examined using Lagergren's pseudo-first-order and McKay's pseudo-second-order kinetic models. The relevant fitting parameters are summarized in Supplementary Figure S1; Supplementary Table S1. The kinetic data for each hydrothermal charcoal showed a better fit with the pseudo-second-order kinetic model (R^2 = 0.999, 0.998, and 0.998) than with the pseudo-first-order kinetic model (R^2 > 0.96 for 30-A-220; R^2 < 0.96 for 52-B-220 and 215–220). This suggests that chemisorption is the primary adsorption mechanism (Li et al., 2019; Rodríguez-Reinoso, 1998).

3.3.3 Adsorption isotherms

To validate the adsorption behavior and assess the adsorption capacity of hydrothermal charcoal, the U(VI) adsorption isotherm was thoroughly examined. The isotherm data were analyzed using the Langmuir and Freundlich adsorption models (Supplementary Figure S2; Supplementary Table S2). The adsorption data for U(VI) on 52-B-220 exhibited a superior fit to the Freundlich adsorption model (R^2 = 0.998) compared to the Langmuir model (R^2 = 0.980), indicating that adsorption occurred as a multilayer process on a heterogeneous surface (Xu et al., 2019). Given that the value of n ranged between 1 and 10, increasing temperature and concentration were favorable for enhancing adsorption performance. For 30-A-220 and 215–220, Supplementary Table S2 shows that the Langmuir model's fitting coefficients (R^2) were all greater than 0.99, slightly outperforming those of the Freundlich model. This indicates that the primary driving force for U(VI) adsorption was point-to-point monolayer adsorption on a homogeneous surface (Im and Choi, 2018).

Additionally, Supplementary Table S3 provides a comparative analysis of the qm values of hydrothermal charcoals from this study and those reported in other studies.

In its unmodified form, 52-B-220 biochar exhibits superior adsorption capacity. This enhanced capacity is attributed to methodological adjustments made in this study, which fully exploit the natural template provided by the raw material's three-dimensional lignin network structure, thereby increasing the specific surface area and pore volume of 52-B-220. Although the adsorption capacity of functionalized biochar exceeds that of 52-B-220, the improvements in physical adsorption in 52-B-220 do not hinder subsequent functionalization processes. Future studies can employ adaptable functionalization processes tailored to specific adsorbates, positioning 52-B-220 as an ideal precursor for further enhancements. The cellulose/lignin adjustment strategy has proven successful, establishing 52-B-220 as a cost-effective, readily available adsorbent, particularly well-suited for large-scale pollution control applications. Moreover, 52-B-220 serves as an outstanding precursor for developing highly efficient adsorbents.

3.3.4 Thermodynamics of adsorption

The results for each hydrothermal charcoal are illustrated in Supplementary Figure S3 and outlined in Supplementary Table S4. The thermodynamic curves and parameters for U(VI) ion adsorption by each hydrothermal charcoal suggest that the process is both spontaneous and endothermic. According to the equation $\Delta G = \Delta H - T\Delta S$, where $\Delta H^\circ > 0$ (endothermic) and $\Delta S^\circ > 0$, the ΔG° values for U(VI) adsorption by each charcoal between 288.15 K and 328.15 K were negative.

3.3.5 Elution/regeneration study

The regeneration study of hydrothermal charcoal is of substantial importance for its practical applications. Following adsorption, biochar can be regenerated by washing with hydrochloric acid, which restores adsorption sites and renders the biochar reusable (Chen et al., 2016). The experiment was performed under optimal adsorption conditions (T = 25°C, t = 6 h, pH = 5, C_0 = 20 ppm, Dose = 0.02 g) (Figure 4). After five cycles, the adsorption capacity of 52-B-220 decreased from 22.58 mg/g to 19.94 mg/g, retaining 86.13% of its original adsorption capacity. The slight reduction in adsorption capacity is attributed to the incomplete desorption of U(VI) ions from the biochar surface. The regeneration results indicate that 52-B-220 is a promising candidate for U(VI) adsorption.

3.3.6 Effect of the coexisting ions

Given the diverse array of coexisting ions in natural wastewater, it is crucial to investigate the selective adsorption of U. Figures 4B, C illustrate that the adsorption capacity and distribution factor of 52-B-220 for U(VI) are 23.35 mg/g and 2.24 L/g, respectively. These values are significantly higher than those for other coexisting ions, indicating that 52-B-220 exhibits strong adsorption affinity and capacity for U(VI), making it a suitable adsorbent for separating U(VI) from multicomponent systems.

3.4 Adsorption mechanism

In order to further clarify the possible adsorption mechanism of U (VI) by the hydrothermal charcoals, the chemical composition, and surficial chemical states of 52-B-220 before and after adsorption are characterized by FTIR, XPS and LSV. As depicted in Supplementary Figure S4, comparison of the FTIR spectra of 52-B-220 (Supplementary Figure S4) revealed a new absorption band at 915 cm^{-1} post-adsorption. This peak technically corresponds to the asymmetric stretching vibration of U (VI) (Quilès and Burneau, 2000; Su et al., 2022). Indicating that uranyl ions were successfully adsorbed onto the surface of 52-B-220. Meanwhile, the FTIR spectra of the adsorbent-before and after adsorption-shows that the peak at 1,696 cm^{-1} slightly shifted to 1703 cm^{-1} after adsorption, what indicates the involvement of -C=O group in the adsorption of U(VI) (Jin et al., 2018); the intensity of peak at 1,205 cm^{-1} decreases after adsorption, suggesting the participation of -OH (phenol) in the adsorption of U(VI) (Liu et al., 2013); and peaks at 1,058 cm^{-1}, 1,110 cm^{-1}, and 1,160 cm^{-1} also decrease after adsorption, indicating the involvement of -OH (alcohol) in the adsorption of U(VI) (Mishra et al., 2017).

Prior to the adsorption of U(VI) ions, the XPS survey spectra of 52-B-220 peaked at 286 eV and 533 eV corresponding to C1s and

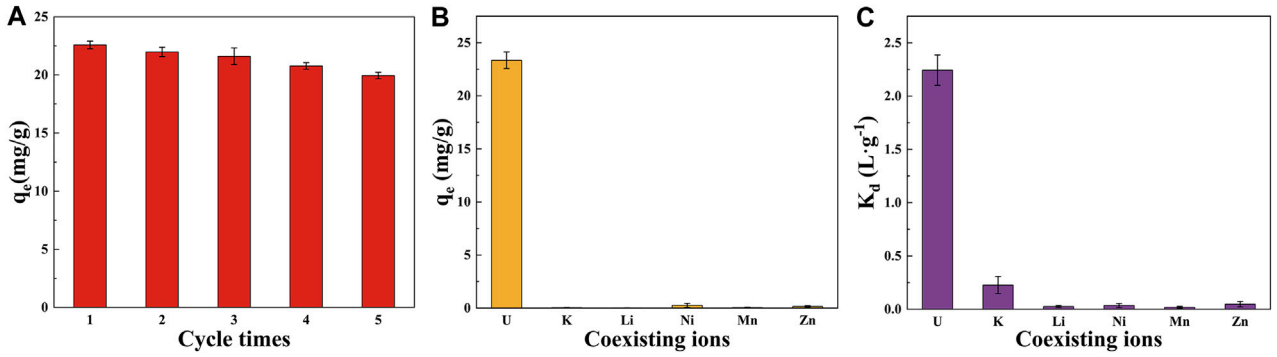

FIGURE 4
(A) Regeneration of U(VI) adsorption on 52-B-220. **(B)** Adsorption capacity and **(C)** distribution factor of 52-B-220 for co-existing ions.

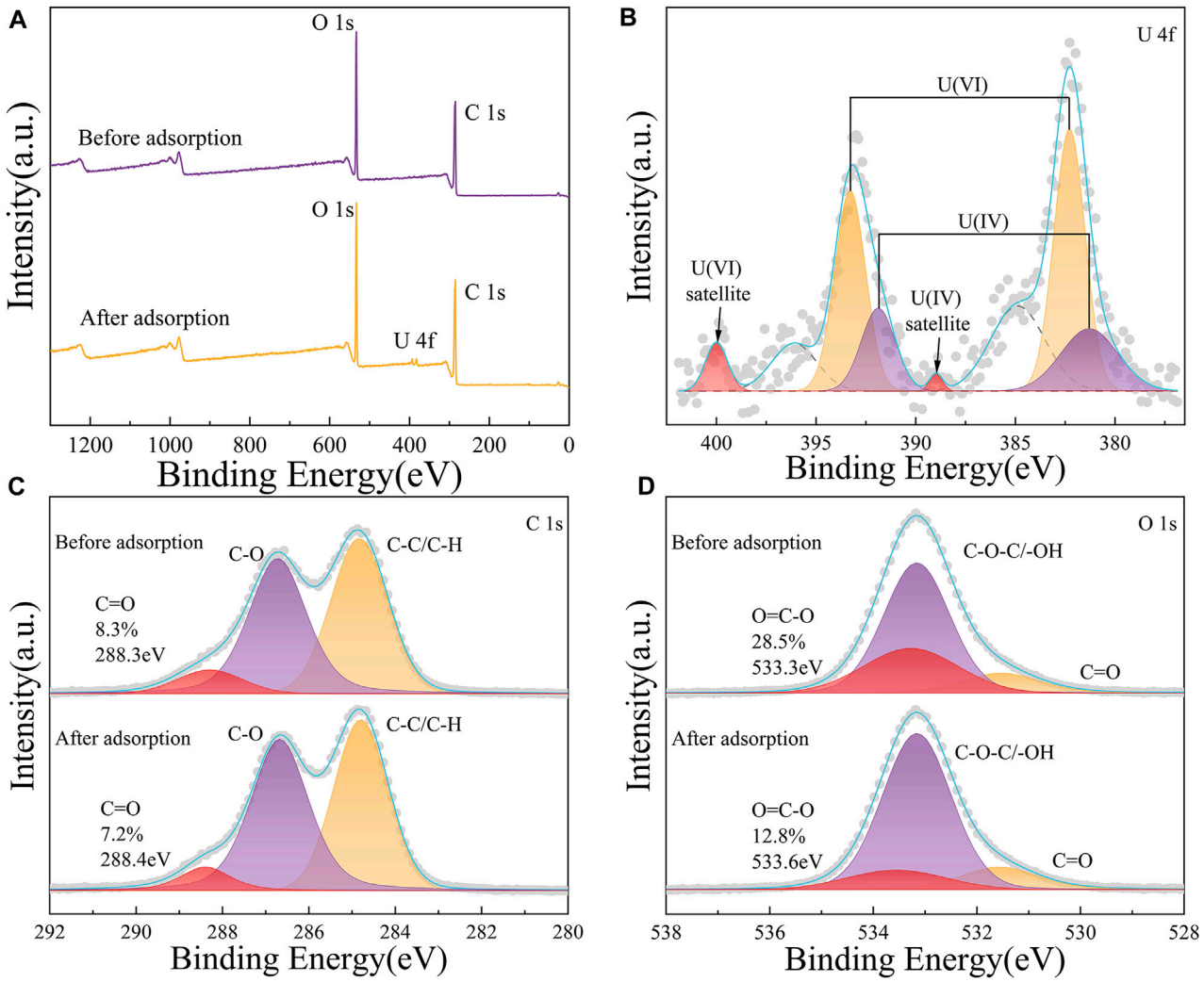

FIGURE 5
XPS spectra of 52-B-220 before and after the adsorption of U(VI) ions: **(A)** XPS survey spectra; **(B–D)** high-resolution XPS spectra of U4f, C1s, and O1s, respectively, obtained post adsorption.

O1s, respectively (Figure 5A). The new peak binding energy at 390eV is attributed to U(VI), implying that U(VI) was successfully adsorbed onto the surface of 52-B-220. Two peaks with binding energies of 382.3 and 393.2 eV are detected in the U 4f spectrum, which are related to U $4f_{7/2}$ and U $4f_{5/2}$ peaks, respectively (Figure 5B). Notably, each of these were deconvoluted to peak at 381.3 eV and 391.9 eV, and 382.3 eV and 393.3 eV, which agreed with U (IV) and U(VI). The satellite peaks of U(VI) $4f_{5/2}$ (400.0 eV), and U(IV) $4f_{7/2}$ (389.0 eV) verified the existence of both U species, implying that some U(VI) was reduced to U(IV) during the processing of the biomass (Ilton and Bagus, 2011; Xiang et al., 2018).

The high-resolution C1s signals were deconvoluted to peak at 284.8 eV (C-C/C-H), 286.7 eV (C-O of hydroxyl and ether), and 288.3 eV (C=O of carboxyl and ester) (Figure 5C) (Biesinger, 2022; Chen et al., 2022; Moeini et al., 2022; Yang et al., 2022). After adsorption, due to the involvement of C=O, the peak at 288.3 eV shifted slightly to 288.4 eV, and its relative intensity decreased. Additionally, the high-resolution O1s signal was deconvoluted to give three peaks located at 531.5 eV (C=O), 533.2 eV (C-O-C/-OH), and 533.3 eV (O=C-O) (Figure 5D). After adsorption, the peaks at 533.3 eV and 531.5 eV shifted to 533.56 eV and 531.6 eV, respectively, due to the participation of O=C-O and C=O; and their relative intensities decreased accordingly. The small shifts in binding energy and decrease in signal intensity of O=C-O and C=O were indicative of their interaction with U(VI) (Chen et al., 2022; Yu et al., 2019; Zhang et al., 2020). Meanwhile, we recorded the linear sweep voltammetry (LSV) curves in the presence of 20ppm U(VI) within a 0.5 M Na+ electrolyte solution (Supplementary Figure S6). In the presence of uranium, two distinct peaks were recorded at −0.67 V and −0.89 V vs. Ag/AgCl, corresponding to the reduction of U(VI) to U(V) and U(V) to U(IV), respectively. These results suggest that the observed processes may occur via electron transfer and coordinate bond formation between the carboxyl and ester groups of 52-B-220 and U(VI).

4 Conclusion

The increase in the cellulose/lignin ratio in *D. farinosus* resulted in enhanced aggregation of carbon microspheres within the hydrothermal biochar, leading to a reduction in specific surface area and pore volume, ultimately resulting in decreased adsorption capacity of the hydrothermal biochar. In comparison to biochar with a high cellulose/lignin ratio, 52-B-220 exhibited a significantly larger specific surface area (an increase of 151.71%) and higher adsorption capacity (an increase of 76.05%), indicating that adjusting raw materials is a viable approach for achieving higher adsorption capacity. Batch adsorption results revealed that the adsorption process of 52-B-220 primarily involved multi-layer endothermic chemisorption. FT-IR and XPS spectra demonstrated that U (VI) adsorption by 52-B-220 mainly occurred through carboxyl and hydroxyl groups. Reducing the cellulose/lignin ratio serves as a fundamental method for enhancing the performance of hydrothermal biochar while reducing post-treatment costs. Modifying the structure of raw materials offers a feasible solution for cost reduction and efficiency improvement in biochar adsorption.

Data availability statement

The original contributions presented in the study are included in the article/Supplementary Material, further inquiries can be directed to the corresponding authors.

Author contributions

FY: Conceptualization, Data curation, Formal Analysis, Investigation, Methodology, Project administration, Software, Validation, Visualization, Writing–original draft, Writing–review and editing. HL: Conceptualization, Supervision, Visualization, Writing–review and editing. BW: Conceptualization, Formal Analysis, Investigation, Project administration, Supervision, Writing–review and editing. WF: Project administration, Supervision, Writing–review and editing. XG: Supervision, Writing–review and editing. YC: Funding acquisition, Project administration, Supervision, Writing–review and editing. SH: Conceptualization, Funding acquisition, Project administration, Resources, Supervision, Writing–review and editing.

Funding

The author(s) declare that financial support was received for the research, authorship, and/or publication of this article. This study was supported by the Science and Technology Project of Sichuan Province, China (2022NSFSC0093 and 2021YFYZ0006), the National Key R&D Program of China (2021YFD2200504_1 and 2021YFD2200505_2), the Ph.D. Foundation of Southwest University of Science and Technology (No. 18zx7128).

Conflict of interest

The authors declare that the research was conducted in the absence of any commercial or financial relationships that could be construed as a potential conflict of interest.

Publisher's note

Supplementary material

The Supplementary Material for this article can be found online at: https://www.frontiersin.org/articles/10.3389/fenvs.2024.1451496/full#supplementary-material

References

Abdi, S., Nasiri, M., Mesbahi, A., and Khani, M. H. (2017). Investigation of uranium (VI) adsorption by polypyrrole. *J. Hazard. Mater.* 332, 132–139. doi:10.1016/j.jhazmat.2017.01.013

Ahmad, M., Rajapaksha, A. U., Lim, J. E., Zhang, M., Bolan, N., Mohan, D., et al. (2014). Biochar as a sorbent for contaminant management in soil and water: a review. *Chemosphere* 99, 19–33. doi:10.1016/j.chemosphere.2013.10.071

Aleeva, S. V., Lepilova, O. V., and Koksharov, S. A. (2020). Study of reducing destruction of lignin by FT-IR spectroscopy. *J. Appl. Spectrosc.* 87, 779–783. doi:10.1007/s10812-020-01069-0

Biesinger, M. C. (2022). Accessing the robustness of adventitious carbon for charge referencing (correction) purposes in XPS analysis: insights from a multi-user facility data review. *Appl. Surf. Sci.* 597, 153681. doi:10.1016/j.apsusc.2022.153681

Chen, L., Zhao, D., Chen, S., Wang, X., and Chen, C. (2016). One-step fabrication of amino functionalized magnetic graphene oxide composite for uranium(VI) removal. *J. Colloid Interface Sci.* 472, 99–107. doi:10.1016/j.jcis.2016.03.044

Chen, Z., He, X., Li, Q., Yang, H., Liu, Y., Wu, L., et al. (2022). Low-temperature plasma induced phosphate groups onto coffee residue-derived porous carbon for efficient U(VI) extraction. *J. Environ. Sci.* 122, 1–13. doi:10.1016/j.jes.2021.10.003

Chen, Z., Liu, T., Tang, J., Zheng, Z., Wang, H., Shao, Q., et al. (2018). Characteristics and mechanisms of cadmium adsorption from aqueous solution using lotus seedpod-derived biochar at two pyrolytic temperatures. *Environ. Sci. Pollut. Res. Int.* 25, 11854–11866. doi:10.1007/s11356-018-1460-1

Cuong, D. V., Matsagar, B. M., Lee, M. S., Hossain, M. S. A., Yamauchi, Y., Vithanage, M., et al. (2021). A critical review on biochar-based engineered hierarchical porous carbon for capacitive charge storage. *Renew. & Sustain. Energy Rev.* 145, 111029. doi:10.1016/j.rser.2021.111029

Deanin, R. D., Driscoll, S. B., Cook, R. J., Dubreuil, M. P., and Shaker, W. A.(1978). Lignin as a filler in commodity thermoplastics.

Domingo, J. L. (2001). Reproductive and developmental toxicity of natural and depleted uranium: a review. *Reprod. Toxicol. (Elmsford, N.Y.)* 15, 603–609. doi:10.1016/s0890-6238(01)00181-2

Elnour, A. Y., Alghyamah, A. A., Shaikh, H. M., Poulose, A. M., Al-Zahrani, S. M., Anis, A., et al. (2019). Effect of pyrolysis temperature on biochar microstructural evolution, physicochemical characteristics, and its influence on biochar/polypropylene composites. *Appl. Sciences-Basel* 9, 1149. doi:10.3390/app9061149

Falco, C., Baccile, N., and Titirici, M.-M. (2011). Morphological and structural differences between glucose, cellulose and lignocellulosic biomass derived hydrothermal carbons. *Green Chem.* 13, 3273–3281. doi:10.1039/c1gc15742f

Fang, Q., Chen, B., Lin, Y., and Guan, Y. (2014). Aromatic and hydrophobic surfaces of wood-derived biochar enhance perchlorate adsorption via hydrogen bonding to oxygen-containing organic groups. *Environ. Sci. Technol.* 48 (1), 279–288. doi:10.1021/es403711y

Fang, R., Lu, C., Zhong, Y., Xiao, Z., Liang, C., Huang, H., et al. (2020). Puffed rice carbon with coupled sulfur and metal iron for high efficiency mercury removal in aqueous solution. *Environ. Sci. Technol.* 54, 2539–2547. doi:10.1021/acs.est.9b07385

Hinck, J. E., Cleveland, D., and Sample, B. E. (2021). Terrestrial ecological risk analysis via dietary exposure at uranium mine sites in the Grand Canyon watershed (Arizona, USA). *Chemosphere* 265, 129049. doi:10.1016/j.chemosphere.2020.129049

Hu, S. L. (2022). *Research on the creation and breeding of new germplasm of cluster bamboo for industrial use: the creation and breeding of new germplasm of* Dendrocalamus farinosus. Beijing: Science Press.

Hui, J. J., Wang, Y. Q., Liu, Y. H., Cao, X. H., Zhang, Z. B., Dai, Y., et al. (2019). Effects of pH, carbonate, calcium ion and humic acid concentrations, temperature, and uranium concentration on the adsorption of uranium on the CTAB-modified montmorillonite. *J. Radioanalytical Nucl. Chem.* 319, 1251–1259. doi:10.1007/s10967-019-06415-x

Humelnicu, D., Blegescu, C., and Ganju, D. (2014). Removal of uranium(VI) and thorium(IV) ions from aqueous solutions by functionalized silica: kinetic and thermodynamic studies. *J. Radioanalytical Nucl. Chem.* 299, 1183–1190. doi:10.1007/s10967-013-2873-4

Ilton, E. S., and Bagus, P. S. (2011). XPS determination of uranium oxidation states. *Surf. Interface Analysis* 43, 1549–1560. doi:10.1002/sia.3836

Im, H.-J., and Choi, K.-S. (2018). Investigation of gaseous wet methyl iodide adsorption on Ag nanoparticles embedded in organic-inorganic hybrid silica gels. *J. Radioanalytical Nucl. Chem.* 316, 1323–1328. doi:10.1007/s10967-018-5866-5

Inyang, M. I., Gao, B., Yao, Y., Xue, Y., Zimmerman, A., Mosa, A., et al. (2016). A review of biochar as a low-cost adsorbent for aqueous heavy metal removal. *Crit. Rev. Environ. Sci. Technol.* 46, 406–433. doi:10.1080/10643389.2015.1096880

Jin, J., Li, S., Peng, X., Liu, W., Zhang, C., Yang, Y., et al. (2018). HNO3 modified biochars for uranium (VI) removal from aqueous solution. *Bioresour. Technol.* 256, 247–253. doi:10.1016/j.biortech.2018.02.022

Kang, X., Kirui, A., Widanage, M. C. D., Mentink-Vigier, F., Cosgrove, D. J., and Wang, T. (2019). Lignin-polysaccharide interactions in plant secondary cell walls revealed by solid-state NMR. *Nat. Commun.* 10, 347. doi:10.1038/s41467-018-08252-0

Lawal, A. A., Hassan, M. A., Zakaria, M. R., Yusoff, M. Z. M., Norrrahim, M. N. F., Mokhtar, M. N., et al. (2021). Effect of oil palm biomass cellulosic content on nanopore structure and adsorption capacity of biochar. *Bioresour. Technol.* 332, 125070. doi:10.1016/j.biortech.2021.125070

Li, M. X., Liu, H. B., Chen, T. H., Dong, C., and Sun, Y. B. (2019). Synthesis of magnetic biochar composites for enhanced uranium (VI) adsorption. *Sci. Total Environ.* 651, 1020–1028. doi:10.1016/j.scitotenv.2018.09.259

Liang, F., Wang, R., Xiang, H., Yang, X., Zhang, T., Hu, W., et al. (2018). Investigating pyrolysis characteristics of moso bamboo through TG-FTIR and Py-GC/MS. *Bioresour. Technol.* 256, 53–60. doi:10.1016/j.biortech.2018.01.140

Liang, Y., Xia, M., Yu, Q., Li, Y., Sui, Z., Yuan, Y., et al. (2022). Guanidinium-based ionic covalent organic frameworks for capture of uranyl tricarbonate. *Adv. Compos. Hybrid Mater.* 5, 184–194. doi:10.1007/s42114-021-00311-3

Liao, J., Xiong, T., Ding, L., Xie, Y., Zhang, Y., and Zhu, W. (2022). Design of a renewable hydroxyapatite-biocarbon composite for the removal of uranium(VI) with high-efficiency adsorption performance. *Biochar* 4, 29. doi:10.1007/s42773-022-00154-1

Liu, C., Huang, X., and Kong, L. Z. (2017). Efficient low temperature hydrothermal carbonization of Chinese reed for biochar with high energy density. *Energies* 10, 2094. doi:10.3390/en10122094

Liu, F., Wang, S., Zhao, C., and Hu, B. (2023). Constructing coconut shell biochar/MXenes composites through self-assembly strategy to enhance U(VI) and Cs(I) immobilization capability. *Biochar* 5, 31–16. doi:10.1007/s42773-023-00231-z

Liu, J., Li, J., Yang, X., Song, Q., Bai, C., Shi, Y., et al. (2013). Facile preparation of polyphenolic hydroxyl functionalized uranium-selective chelating sorbent: simple oxidation of styrene-divinylbenzene copolymer microparticles by Hummers method. *Mater. Lett.* 97, 177–180. doi:10.1016/j.matlet.2013.01.120

Mishra, S. P., Tiwari, D., Prasad, S. K., Dubey, R. S., and Mishra, M. (2006). Inorganic ion-exchangers in radioactive waste management</p> </p>: Part XVI: uptake of some metal phosphates (stannic and zirconium) for 134Cs</p> </p>. *J. Radioanalytical & Nucl. Chem.* 268, 191–199. doi:10.1556/JRNC.268.2006.2.3

Mishra, V., Sureshkumar, M. K., Gupta, N., and Kaushik, C. P. (2017). Study on sorption characteristics of uranium onto biochar derived from Eucalyptus wood. *Water Air Soil Pollut.* 228, 309. doi:10.1007/s11270-017-3480-8

Moeini, B., Linford, M. R., Fairley, N., Barlow, A., Cumpson, P., Morgan, D., et al. (2022). Definition of a new (Doniach-Sunjic-Shirley) peak shape for fitting asymmetric signals applied to reduced graphene oxide/graphene oxide XPS spectra. *Surf. Interface Analysis* 54, 67–77. doi:10.1002/sia.7021

Quilès, F., and Burneau, A. (2000). Infrared and Raman spectra of uranyl(VI) oxo-hydroxo complexes in acid aqueous solutions: a chemometric study. *Vib. Spectrosc.* 23, 231–241. doi:10.1016/S0924-2031(00)00067-9

Rodríguez-Reinoso, F. (1998). The role of carbon materials in heterogeneous catalysis. *Carbon* 36, 159–175. doi:10.1016/s0008-6223(97)00173-5

Sevilla, M., and Fuertes, A. B. (2009). The production of carbon materials by hydrothermal carbonization of cellulose. *Carbon* 47, 2281–2289. doi:10.1016/j.carbon.2009.04.026

Su, Y., Wenzel, M., Paasch, S., Seifert, M., Doert, T., Brunner, E., et al. (2022). One-pot synthesis of brewer's spent grain-supported superabsorbent polymer for highly efficient uranium adsorption from wastewater. *Environ. Res.* 212, 113333. doi:10.1016/j.envres.2022.113333

Titirici, M. M., Antonietti, M., and Baccile, N. (2008). Hydrothermal carbon from biomass: a comparison of the local structure from poly-to monosaccharides and pentoses/hexoses. *Green Chem.* 10, 1204–1212. doi:10.1039/b807009a

Tong Thi, P., Ma, Z., Chen, D., and Zhang, Q. (2014). Pyrolysis characteristics and kinetics study of bamboo holo-celluloce using TG-FTIR. *J. Zhejiang a&f Univ.* 31, 495–501. doi:10.11833/j.issn.2095-0756.2014.04.001

Wegener, M., Eppinger, T., Baeumler, K., Kraume, M., Paschedag, A. R., and Baensch, E. (2009). Transient rise velocity and mass transfer of a single drop with interfacial instabilities-Numerical investigations. *Chem. Eng. Sci.* 64, 4835–4845. doi:10.1016/j.ces.2009.07.023

Wu, X., Ba, Y., Wang, X., Niu, M., and Fang, K. (2018). Evolved gas analysis and slow pyrolysis mechanism of bamboo by thermogravimetric analysis, Fourier transform infrared spectroscopy and gas chromatography-mass spectrometry. *Bioresour. Technol.* 266, 407–412. doi:10.1016/j.biortech.2018.07.005

Xiang, S., Cheng, W., Nie, X., Ding, C., Yi, F., Asiri, A. M., et al. (2018). Zero-valent iron-aluminum for the fast and effective U(VI) removal. *J. Taiwan Inst. Chem. Eng.* 85, 186–192. doi:10.1016/j.jtice.2018.01.039

Xu, W., Zhang, W., Kang, J., and Li, B. (2019). Facile synthesis of mesoporous Fe-based MOFs loading bismuth with high speed adsorption of iodide from solution. *J. Solid State Chem.* 269, 558–565. doi:10.1016/j.jssc.2018.10.028

Yang, H., Huang, L., Liu, S., Hou, M., Sun, K., and Sun, Y. (2017). Study on bamboo pyrolysis process and product characteristics. *Acta Energiae Solaris Sin.* 38, 1431–1439.

Yang, W., Peng, D., Kimura, H., Zhang, X., Sun, X., Pashameah, R. A., et al. (2022). Honeycomb-like nitrogen-doped porous carbon decorated with Co_3O_4 nanoparticles for superior electrochemical performance pseudo-capacitive lithium storage and supercapacitors. *Adv. Compos. Hybrid Mater.* 5, 3146–3157. doi:10.1007/s42114-022-00556-6

Yu, J., Yuan, L., Wang, S., Lan, J., Zheng, L., Xu, C., et al. (2019). Phosphonate-Decorated covalent organic frameworks for actinide extraction: a breakthrough under highly acidic conditions. *J. Chin. Chem. Soc.* 003, 286–295. doi:10.31635/ccschem.019.20190005

Yu, L. H., Falco, C., Weber, J., White, R. J., Howe, J. Y., and Titirici, M. M. (2012). Carbohydrate-derived hydrothermal carbons: a thorough characterization study. *Langmuir* 28, 12373–12383. doi:10.1021/la3024277

Zanon Costa, C., Falabella Sousa-Aguiar, E., Peixoto Gimenes Couto, M. A., and Souza de Carvalho Filho, J. F. (2020). Hydrothermal treatment of vegetable oils and fats aiming at yielding hydrocarbons: a review. *Catalysts* 10, 843. doi:10.3390/catal10080843

Zhang, S., Yuan, D., Zhang, Q., Wang, Y., Liu, Y., Zhao, J., et al. (2020). Highly efficient removal of uranium from highly acidic media achieved using a phosphine oxide and amino functionalized superparamagnetic composite polymer adsorbent. *J. Mater. Chem. A* 8, 10925–10934. doi:10.1039/d0ta01633k

Zhao, W. H., Lin, X. Y., Cai, H. M., Mu, T., and Luo, X. G. (2017). Preparation of mesoporous carbon from sodium lignosulfonate by hydrothermal and template method and its adsorption of uranium(VI). *Industrial & Eng. Chem. Res.* 56, 12745–12754. doi:10.1021/acs.iecr.7b02854

Zhu, L., and Zhong, Z. (2020). Effects of cellulose, hemicellulose and lignin on biomass pyrolysis kinetics. *Korean J. Chem. Eng.* 37, 1660–1668. doi:10.1007/s11814-020-0553-y